Physical Biology

OFFICIAL JOURNAL OF
Sociedad de Biofísicos Latino Americanos

PAPER • OPEN ACCESS

Replicating landmine blast loading in cellular *in vitro* models

To cite this article: David R Sory *et al* 2020 *Phys. Biol.* **17** 056001

Physical Biology

OPEN ACCESS

PAPER

Replicating landmine blast loading in cellular *in vitro* models

David R Sory[1,2,4,5], Harsh D Amin[2,4], David J Chapman[1,3], William G Proud[1,4] and Sara M Rankin[2,4]

[1] Institute of Shock Physics, Department of Physics, Imperial College London, London SW7 2AZ, United Kingdom
[2] National Heart & Lung Institute, Faculty of Medicine, Imperial College London, London SW7 2AZ, United Kingdom
[3] Department of Engineering Science, University of Oxford, Oxford OX1 3PJ, United Kingdom
[4] The Royal British Legion—Centre for Blast Injury Studies, Imperial College London, London SW7 2AZ, United Kingdom
[5] Address for correspondence: Dr David Sory, National Heart & Lung Institute, Faculty of Medicine, Imperial College London, South Kensington Campus, SW7 2AZ.

E-mail: d.sory14@imperial.ac.uk

RECEIVED
21 November 2019

REVISED
19 February 2020

ACCEPTED FOR PUBLICATION
5 March 2020

PUBLISHED
11 August 2020

Keywords: stem cell, blast injuries, osteogenesis, anti-personnel landmine, periosteum, split-Hopkinson pressure bar, strain rate

Supplementary material for this article is available online

Abstract

Trauma arising from landmines and improvised explosive devices promotes heterotopic ossification, the formation of extra-skeletal bone in non-osseous tissue. To date, experimental platforms that can replicate the loading parameter space relevant to improvised explosive device and landmine blast wave exposure have not been available to study the effects of such non-physiological mechanical loading on cells. Here, we present the design and calibration of three distinct *in vitro* experimental loading platforms that allow us to replicate the spectrum of loading conditions recorded in near-field blast wave exposure. We subjected cells in suspension or in a three-dimensional hydrogel to strain rates up to 6000 s^{-1} and pressure levels up to 45 MPa. Our results highlight that cellular activation is regulated in a non-linear fashion—not by a single mechanical parameter, it is the combined action of the applied mechanical pressure, rate of loading and loading impulse, along with the extracellular environment used to convey the pressure waves. Finally, our research indicates that PO MSCs are finely tuned to respond to mechanical stimuli that fall within defined ranges of loading.

1. Introduction

It is generally accepted that the world's landmine and improvised explosive device (IED) threat is reaching crisis level. Explosive devices have become the weapons of choice of non-state armed groups, state actors as well as isolated suicide bombers to incapacitate, maim or kill with an estimated 15 000 to 20 000 annual casualties in open war and low-intensity conflicts [1, 2].

In the recent operational theaters of Iraq and Afghanistan, injury to limbs accounted for more than 8 of every 10 combat wounds due to explosive devices [3, 4]. In 64% of amputees that have lost limbs through IEDs and landmines, heterotopic ossification (HO) is reported [5–8]. Blast-mediated HO is the formation of ectopic bone due to inappropriate mesenchymal stromal cell (MSC) osteogenesis in non-skeletal tissues. Along with systemic factors, recent data have indicated that HO initiates from the local biochemical and biomechanical effects at the injury site [7]. The etiology of blast-mediated HO in IED/landmine trauma remains the subject of much research.

It is well known in the fields of cell biomechanics and mechanobiology that cells actively sense and respond to mechanical forces by modulating a variety of cellular functions, such as stimulating osteogenesis in MSCs. Experimental platforms investigating the mechanical stimulation of osteogenesis have been developed to apply low-intensity pulsed stimuli that recapitulate daily physical activities, such as walking, running or jumping [9–11]. These occur under physiological strain rates, typically from 0.01 to 1 s^{-1}. Blast loadings, however, involve more impulsive events that occur under a broader range of strain rates, from 10 s^{-1} to 10^3 s^{-1} and beyond (figure 1(a)).

A desire to examine how physical forces associated with blast loading cause unprecedented injuries has motivated the development of *in vitro* and *in vivo* models to examine the blast-induced biomechanical and molecular changes in tissues and cells. To

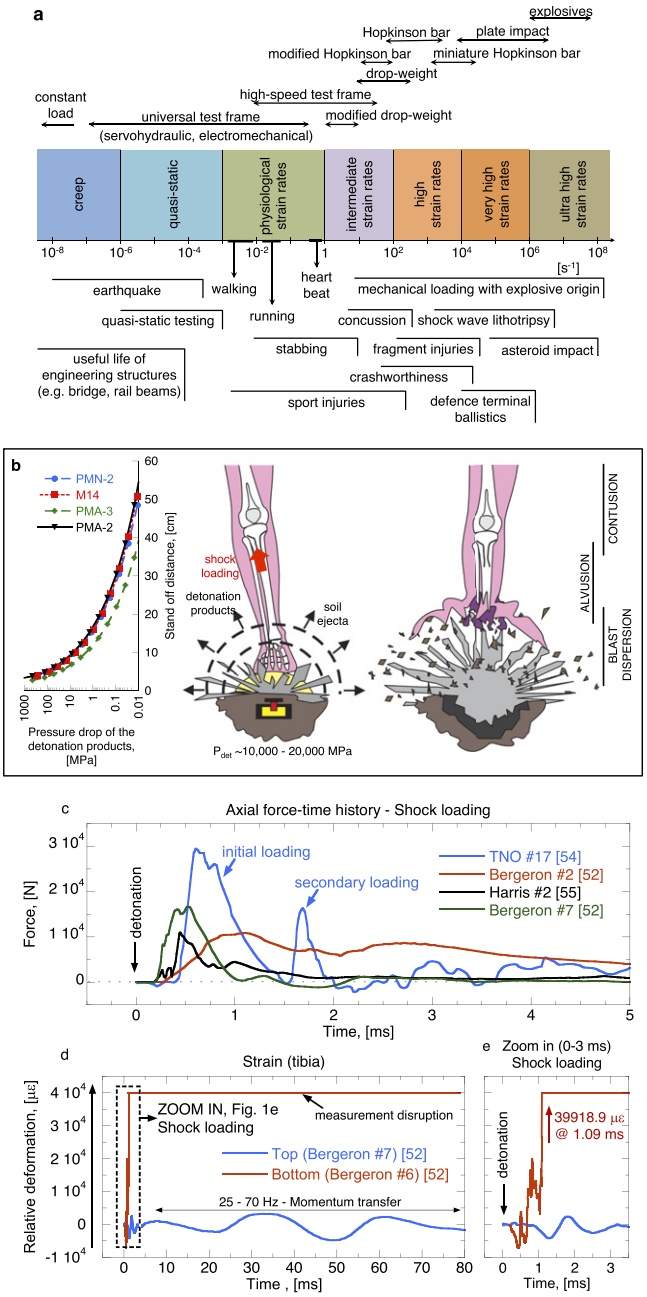

Figure 1. Strain rate map and IED/landmine loading processes. (a) Deformation processes and experimental techniques associated with different ranges of strain rates, from 10^{-8} to 10^{8} s^{-1}. Conventionally, strain rates at or below 10^{-3} s^{-1} are considered to represent quasi static deformations. Strain rates from 10^{-3} s^{-1} up to 1 s^{-1} represent physiological strain rates. These characterise deformation processes occurring in daily-life physical activities, such as walking, running, jumping. Strain rates above 1 s^{-1} are generally qualified as dynamic loadings. The intermediate strain rates range from 1 s^{-1} to 100 s^{-1} and cover most deformation processes occurring in sport injuries, concussion and blunt trauma. Strain rates above 100 s^{-1} are called high strain rates and characterise loading scenarios taking place in road traffic accidents and fragment injuries. (b) Mechanisms of injury in IED/landmine loading processes. In blast events, the processes are so fast that heat transfer is minimal and that the expansion of the detonation products is governed by adiabatic processes. As the blast wave expands, the pressure quickly drops from 1000 MPa at a few centimetres above the detonation seat to 1 MPa peak pressure at around 20 cm. (c) Examples of axial force–time histories measured in lower limbs using load cells and strain gauges during IED/landmine loading processes. Data digitalized from [40, 53, 54]. (d, e) Examples of relative deformation of the top and bottom parts of the tibia in IED/landmine loading processes. The maximum peak deformation can peak up to 40 000 microstrains and cover a broad range of frequencies during the shock loading (high frequencies) and the momentum transfer (low frequencies). Data digitalized from [40].

date, cellular biomechanics of blast has principally focused on primary blast injuries affecting the hearing [12–14], the pulmonary [15] or the central nervous systems [16–19]. At the tissue and cellular levels, contemporary experimental systems for evaluating blast wave exposure include pressure-based platforms [20], modified shock tube systems [21–25], barochambers [26], microfluidic devices [27, 28], atomic force microscopy technique-based systems [29, 30], Kolsky bars [31–34], and laser-based systems [35]. However, blast research has rarely focused on the pathophysiology of landmine/IED trauma on cells

due to the limited availability of test-rigs capable of recreating the relevant mechanical conditions. As a consequence, a paucity of investigations exists into the changes of behavior of surviving tissues and cells from IED/landmine trauma. Experimental *in vitro* platforms that permit exposure of cells in 3D cultures to the biomechanical conditions of IED/landmine trauma would be a significant addition to the repertoire of cell injury devices.

In this study, we present the development and calibration of three experimental biocompatible *in vitro* loading platforms designed to produce biomechanically relevant mechanical loadings of pressures up to 45 MPa, and strain rates from physiological (0.01 s^{-1}) to traumatic (>6000 s^{-1}). We use these platforms to apply mechanical insults mimicking landmine/IED blast wave exposure to periosteum-derived mesenchymal stromal cells (PO MSCs) in liquid suspension culture or homogeneously immobilized a simplified three-dimensional (3D) hydrogel scaffold. We use agarose hydrogel of 1% (w/v) final concentration to produce scaffolds of compressive modulus falling within the range of figures reported for muscle tissue. Post-loading, we monitor cell viability and investigate the expression of the Runx2 mRNA transcription factor, as a measure of cellular activation relevant to MSC differentiation. We show that cell health is not affected by single-pulse loadings of wide range of impulse levels (0.20–95 000 N s). Our data show that there are conditions of strain rate and impulse that activate the expression of the Runx2 mRNA, but importantly that mechanical stimuli of the same peak pressure intensity (but different pulse duration, strain rate regime and loading impulse) did not consistently induce similar levels of upregulation of Runx2 mRNA in PO MSCs. The level of Runx2 mRNA expression increased when PO MSCs were mechanically loaded in a 3D hydrogel scaffolds as compared to those loaded in single-cell liquid suspensions, showing that the stiffness of the environment impacts on the biological response to loading. Overall our results indicate that PO MSCs are finely tuned to respond to mechanical stimuli that fall within these defined ranges of loading, but that the extent cellular activation is not directly related to a single mechanical parameter, but rather the combined action of several features of these traumatic loadings.

2. Landmine blast loading

2.1. Landmine and IED mechanical loading

There are three major contributing injury mechanisms coming from the detonation of IEDs/landmines: (1) the shock loading, (2) the fragment loading coming from the threat casing and surrounding debris, and (3) the momentum transfer from the expanding explosive products [36]. Because of the short range of action, the three mechanisms are thought to occur almost simultaneously [37].

2.1.1. The shock loading

Upon detonation, the high-pressure blast wave with its predominant high frequencies easily penetrates into the body as a shock loading, causing shattering of the hard and the soft tissues in a process known as brisance [38]. As it propagates, the shock loading turns into longitudinal, transverse and surface stress waves traveling at the speed of sound in various anatomical compartments of different acoustic impedance [37] (figure 1(b)). Within a few hundred microseconds, the stress waves will have traveled from the detonation seat through the skin, the bones, the periosteum, the bone marrow, the muscles, the tendons and ligaments up to the tibial plateau, with minimal displacement of the limb [37]. The anatomical structures containing fluid, like arteries and veins, are also subjected to hydrodynamic force to flowing incompressible fluid [39]. The physical and geometrical dissimilarities between adjacent tissues cause longitudinal and shear stresses, resulting in strain and ultimately energy deposited in the soft and hard tissues. This leads to various degrees of damage including tissue lacerations, contusions, stratification, haemorrhages, abrasion, bone micro-fractures and cellular disruption [39]. Because of their high pressure and their high particle velocity, the blast-born stress waves preserve their destructive properties within a certain distance causing damage and contusions to tissues and internal organs further up the limb [40].

2.1.2. The fragment loading

As the detonation processes occur, the casing swells due to the high-pressure developed by the expanding gaseous products. During this very violent acceleration, cracks initiate and propagate into the casing until fragments are formed [41]. The detailed formulations of the fragmentation processes are complex, but the number and size of fragments from a metallic casing can be predicted based on the Mott fragmentation criteria [42]. Just before the casing fracture, the initial velocity imparted to the driven fragments can be predicted using the Gurney model, as shown below for a cylindrical warhead [43].

$$V_G = \sqrt{2E_G}\left(\frac{C/M}{1+0.5C/M}\right)^{1/2} \quad (1a)$$

where V_G is the Gurney initial velocity, $\sqrt{2E_G}$ is the empirical Gurney constant, M and C are the mass of the accelerated casing and the explosive charge, respectively (see supplementary .xls file for examples of predicted peak fragment velocities, available at stacks.iop.org/JPPB/17/056001/mmedia). As the energized fragments penetrate the body, they push through the soft biological tissues, both transferring kinetic energy and loosing energy in

Table 1. Examples of JWL parameters for high-explosives used in commercially available landmines.

Explosive	A, (Mbar)	B, (Mbar)	C, (Mbar)	R_1, (-)	R_2, (-)	ω, (-)
TNT[a]	3.71213	0.032306	0.0104527	4.15	0.95	0.34
HMX[b]	7.7830	0.070710	0.00643	4.20	1.00	0.30
Tetryl[b]	5.8680	0.106710	0.00774	4.40	1.20	0.28
CompB[a]	5.24229	0.076783	0.010818	4.20	1.10	0.35

[a]sourced from Lee *et al* [46].
[b]sourced from Lee *et al* [47].

Table 2. Examples of mechanical loading conditions in landmine/IED blast loading. The data were recorded on instrumented anthropomorphic legs and post-mortem human subjects (PMHS) legs tested in real open field blast loadings (Abr. FSLL: frangible surrogate lower leg; FSL: frangible surrogate leg, CLL: Canadian lower leg, FSLM: frangible surrogate leg modified).

Threat	Leg model	Peak force (kN)	Loading rate (kN ms^{-1})	Axial stress (MPa)	Time to peak force (ms)	Loading impulse to peak force (kN ms)	Ref
PMA-3 VS50	FSL	10.9–20.9	19.1–101.7	54–104	0.26–0.85	1.55–8.39	[40]
M14	FSL	19.2–24.6	31–46	95–122	0.26–0.80	1.55–8.66	[52]
25, 50 or 75 g C4	FSLL, CLL	3.8–29.8	5.8–198.5	19–148	0.21–0.69	2.71–7.46	[53]
landmine	PMHS	3.9–11.0	12.8–137.7	19–55	0.25–1.25	0.61–4.39	[54]
50 g PE4	FSLM	13.2–43.4	53–270	66–216	N/A	N/A	[55]
M-14, PMA-2, PMN AP	PMHS	2.5–15	5–120	12–75	N/A	N/A	[56]

cutting a path, causing the projectiles to slow down [44]. When the explosive device is buried, the superheated, high-pressure gas bubble expanding in the soil breaks through the soil cap and jets out at supersonic speed soil ejecta and surrounding debris. This produces an additional violent stream of particles that extends the severity of the trauma in distorting, lacerating and crushing the various anatomical structures previously damaged by the shock loading [38, 45].

2.1.3. The momentum transfer

The third major effect is due to the range of dynamic pressure coming from the expanding gaseous products, and the resulting momentum imparted by the accelerative and decelerative forces to the damaged limb. In very close proximity to the detonation seat, it is generally fair to assume that the blast processes are so fast that heat transfer is minimal, and thereby that the volumetric expansion of the detonation products is governed by adiabatic processes. These processes are commonly described using a relatively simple pressure, volume, energy equation of state developed by Jones–Wilkins–Lee (JWL), expressed as [46, 47]:

$$P_{\mathrm{det}} = A\mathrm{e}^{-R_1 V} + B\mathrm{e}^{-R_2 V} + \frac{C}{V^{\omega+1}} \qquad (1b)$$

where A, B, R_1, R_2 and ω are high-explosive material constants, P_{det} is the pressure of the detonation product, V is the relative volume. Examples of JWL parameters of various high-explosives are presented in table 1.

Figure 1(b) shows examples of JWL pressure drop as a function of the volumetric expansion of the detonation products with distance for various types of commercially available landmines. An enhancement factor of 1.8 taking into account the contact with the ground was used to convert the adiabatic free-air burst to a surface burst [48]. The model suggests that the expected values of dynamic pressure, which ranges from 100 MPa at 5 cm, and only drops to 0.5 MPa at 15 cm, remain extremely high within the distance that lower extremities normally occupy. These conditions are sufficient to induce varying degrees of displacement, and cause additional bending stresses and torsion [38, 49]. The net result is a brutal dispersion of the crushed soft tissues which is often accompanied by either a total or subtotal amputation of the limb at variable anatomical levels [50, 51].

2.2. Framework of the proposed laboratory experimental technique

In this research, we aim to develop a laboratory experimental technique to investigate the effect of the shock loading at the tissue and cellular level. The framework of the proposed method relies on the use of available experimental data obtained from blast trials using IEDs, explosive charges or commercially available landmines on lower limbs [52–56]. Generally, published data include the force and the relative deformation-time histories inferred from fitted

load cells or strain gauges bonded on the bones of post-mortem human subjects (PMHS) or anthropomorphic leg models (mechanical legs and frangible legs) (figures 1(c)–(e)). We directly used these data as they became available, or have digitalized and further post-processed them to obtain the relevant mechanical parameters (see supplementary .xls file). Table 2 summarizes and presents the analyzed data in terms of loading rate and peak axial force, loading duration, loading impulse, strain as well as range of mechanical stress. Because of the upward and radial field pattern of the blast forces during the loading, we preferentially analyzed the mechanical conditions recorded along the longitudinal axis of the body. The data reveal that the range of axial force varies from 2.5 kN up to 43.4 kN. The rate at which the axial force is applied during the shock loading can reach 270 kN ms^{-1}. In some cases, the shock loading can be featured with secondary loadings [visible in the TNO #17 curve, on figure 1(c)]. Depending on the loading profile, the loading impulse delivered to the samples ranges from approximately 0.61 N s to 8.66 N s at the peak loading. In general, the shock loading is very short and impulsive. The axial force peaks very shortly after the detonation, within a time-period between 210 μs to around 1.25 ms. The data show that the different portions of the loaded bone experience a range of frequencies, from 10^1 s^{-1} up to figures as high as 10^4 s^{-1} during the compressive phase of the loading (figures 1(d) and (e)).

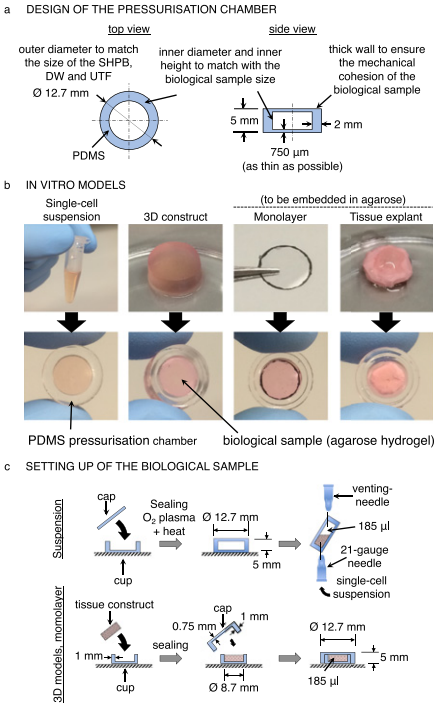

Figure 2. Design of the pressurization chamber. (a) Design criteria of the pressurization chamber (b) Cellular *in vitro* models used in the pressurization chamber. (c) Manufacture of the pressurization chamber, and setting up of the biological samples.

3. *In vitro* platforms for IED/landmine blast trauma

3.1. Design concept

The *in vitro* platforms applied mechanical compressive loading mimicking blast trauma to biological cells cultured in various *in vitro* models. The primary goals of the *in vitro* platforms were: (1) adapting existing laboratory-based mechanical loading apparatus to replicate of the mechanical characteristics of well-defined regions of IED/landmine loadings; (2) interfacing live biological samples with the loading apparatus whilst complying with requirement of sterility and biocompatibility; (3) performing the confined compression of live biological samples under controlled mechanical conditions (e.g. magnitude and duration) relevant to IED/landmine loadings; (4) guaranteeing the recovery of the biological samples after a single-impact loading event in order to correlate their response to the mechanical loading history.

The *in vitro* platforms consisted of the integration of a modified drop-weight rig (DW), and a split-Hopkinson pressure bar (SHPB) as these cover the ranges of strain rates associated with dynamic and traumatic events. A universal testing machine (UTF) was also incorporated in order to cover the physiological range of strain rates and, thus, constituted a baseline for the dynamic experiments. Taken together, these platforms could generate compressive loadings from tens of microseconds to seconds time duration and force intensities up to several thousands Newtons. The *in vitro* platforms were also designed to accommodate a pressurization chamber used to position and hold on the different loading apparatus various *in vitro* models used for cell growth. In their conventional usage, the SHPB and DW systems generally give rise to uncontrolled secondary loadings: wave reverberations on the SHPB and rebound impacts on the DW. In this study, the loading apparatus were therefore mounted with momentum capture systems to ensure the delivery of a single-impact loading, and to guarantee the recovery of the sample under controlled conditions.

3.2. Development of a pressurization chamber

The pressurization chamber allowed the biological samples to be consistently positioned on the *in vitro* platforms. The primary design parameters of the pressurization chambers were: (1) the high-efficiency transmission of the stress pulses from the loading apparatus to the biological sample; (2) to act as a physical barrier and, thus, keep the biological sample under sterile conditions during the compressive loading; (3) to preserve the mechanical integrity of the biological sample throughout the successive steps of the experimentation.

Table 3. Acoustic impedance characterisation. Summary of the bulk density, longitudinal sound speed and acoustic impedance characteristics of polydimethylsiloxane (PDMS), agarose 1% (wt/v) and water.

Parameter	ρ, (g cm^{-3})	c_L, (mm μs^{-1})	Z, (kg m^{-2} s^{-1})[b]
PDMS	0.993 ± 0.0009	1.047 ± 0.0005	$(1\,039 \pm 1.4)\ 10^3$
Agarose 1% (wt/v)	1.011 ± 0.0000	1.495 ± 0.0004	$(1\,511 \pm 0.4)\ 10^3$
Water[a]	1.053	1.490	1 568

[a]Extracted from [61]. Data expressed as mean ± SD.
[b]Mean ± u, with u determined by error propagation analysis.

The pressurization chamber consisted of the tight-fitting assembly of a cup and a cap producing a hermetically sealed cylindrical volume. The cylindrical shape made the mounting consistent across the different loading apparatus. Figure 2(a) depicts the different parts of the chambers and their nominal dimensions. The design of the pressurization chamber accommodates all the contemporary *in vitro* models for cell and tissue studies: (1) single-cell liquid suspension; (2) 3D hydrogel scaffold; (3) tissue explant; (4) cell monolayer on coverslip (figure 2(b)). In this research we proposed agarose hydrogel as 3D scaffold to encapsulate cells, tissue explants and cell monolayer on coverslip. For the liquid suspension model, the biological sample is introduced in the chamber after the sealing and bonding of the cap and cups. In the other models, the chamber is sealed after the biological sample is fit in the cup (figure 2(c)). We manufactured the pressurization chamber from polydimethylsiloxane (PDMS, Sylgard 184 kit, Dow Corning Co., Midland, MI, USA). PDMS is a well-known transparent, cost-effective and non-toxic silicone elastomer widely used in biological assays [57–59]. One interesting characteristic of PDMS was the control of its mechanical properties through the ratio of its mixing components [60]. Most importantly, its acoustic impedance characteristics close to water and high-content water substrates (e.g. agarose hydrogel) made it an attractive candidate for the efficient transmission of the stress waves across the chamber-sample interface [61].

3.3. Acoustic impedance and wave transmission across boundaries

We quantified the acoustic impedance mismatch between the PDMS chamber and the biological sample to determine how much of the stress wave was transmitted and how much was reflected at their interface. For this purpose, we built and used high-accuracy measurement rigs of defined thicknesses for the ultrasonic and bulk density evaluations of PDMS and agarose hydrogel materials (appendix 1 (appendices available in the supplementary material)). Table 3 summarizes the bulk density, sound speed and acoustic impedance charateristics of PDMS, agarose 1% (wt/v) and water. We found reflection ratios of 0.034 ± 0.001 and 0.041 ± 0.001 for the pairs '*PDMS-agarose*' and '*PDMS-water*', respectively.

3.4. *In vitro* sample fixtures

3.4.1. Confinement sleeve

During the compressive loading, the pressurization chamber containing the biological sample was placed in a tight-fitting cylindrical confining sleeve to provide a restraint against its radial expansion, and thereby to generate a multiaxial stress state within the biological sample. The inner diameter of the confining sleeve was 12.7 mm to match the outer diameter of the pressurization chamber. The confining sleeve was made of AISI 316L Stainless Steel ($\sigma_y = 205$ MPa and $E = 193$ GPa, $\rho = 7\,850$ kg m^{-3}). It was also mounted with a strain gauge (type AFP-900-050, Kulite, Basingstoke, UK) arranged on the outer surface and with the active element normal to the centerline in order to acquire the circumferential strain. The confining sleeve was connected to a Wheatstone bridge, and the external circumferential strain was recorded in terms of strain gauge voltage output on a digital oscilloscope (at 2.5 MS s^{-1} on Tektronix, type DPO3034, Portland Oregon, USA). The calibration relationship between the output voltage and the strain was empirically determined by subjecting the sleeve to a radial loading, and then solving the circumferential strain distribution using the analytical solution of circular ring subjected to two equal forces acting along the diameter [62] (appendix 2 in the supplementary material). The external radial stress was related to the external circumferential strain using the reduced formulation from the thick wall theory, as:

$$\sigma_\theta = \frac{E_{sl}}{2R_i^2}\left(R_e^2 - R_i^2\right)\varepsilon_\theta \qquad (2)$$

where E_{sl} is the elastic modulus of the confining sleeve material, ε_θ is the external circumferential strain, R_i and R_e are the internal and external radius of the confining sleeve, respectively.

3.4.2. The loading cap

In the DW and UTF experiments, we used a 12.7 mm diameter loading cap to transfer the axial load from the impactor (DW) or the crosshead (UTF) to the pressurization chamber. The loading cap was mounted with a strain gauge arranged with the active element parallel to the centerline in order to acquire axial loading. Similar to the confining sleeve, the loading cap was connected to a Wheatstone bridge, and the axial force was recorded in terms of strain gauge

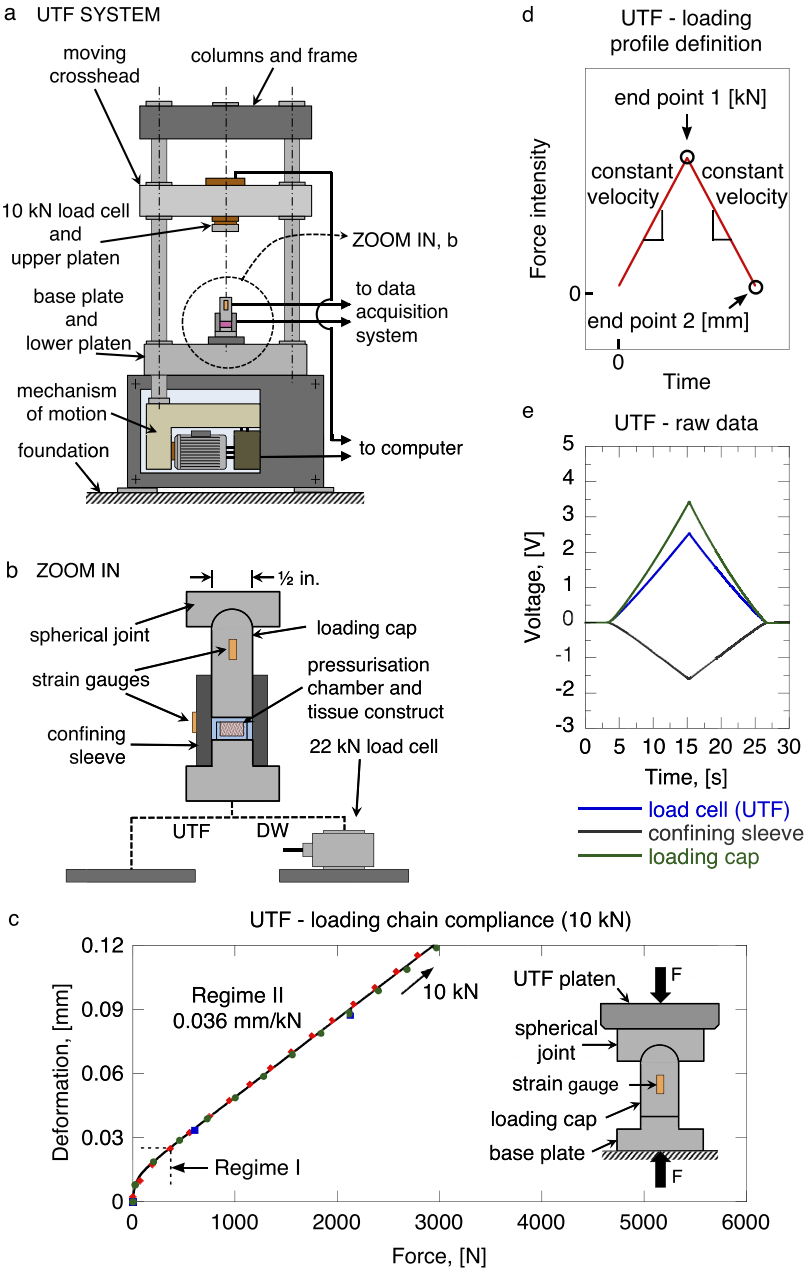

Figure 3. Physiological strain rate loadings. (a) Schematic of the universal test frame (UTF) and its diagnostics. (b) Mounting of the pressurization chamber and the confining sleeve. (c) Non-linearities in the loading chain. (d) Definition of the UTF profile. (e) Example of raw data.

voltage output on a digital oscilloscope. The calibration relationship between the voltage output and the applied axial force was determined by subjecting the loading cap to a series of compression-release cycles on a UTF (Instron, model 5866, Buckinghamshire, UK) (appendix 2). The loading cap was made of AISI 316L Stainless Steel ($\sigma_y = 205$ MPa and $E = 193$ GPa, $\rho = 7\ 850$ kg m^{-3}) and was used within its elastic domain.

3.5. *In vitro* loading platform

3.5.1. Physiological strain rate regime

We performed the low strain rate compressive loadings on a UTF (figure 3(a)). The loading apparatus was instrumented with a 10 kN force load cell, and a built-in positional control system to acquire the force–time and the displacement–time histories, respectively. We ensured platen parallelism by using a lubricated, self-aligning spherical joint on the top of the loading cap (figure 3(b)). The force–time and displacement–time histories were recorded on the Instron BlueHill2 software at a sampling rate of 1 Hz. For all compressive loadings, we corrected for loading compliance by subtracting the non-sample displacement in the load chain from the total displacement (figure 3(c)). We generated triangular loading pulses of different force intensity and time duration by controlling the force end-point and the loading rate of the crosshead (figures 3(d) and (e)). Because the displacements of the crosshead were very small, we decided to

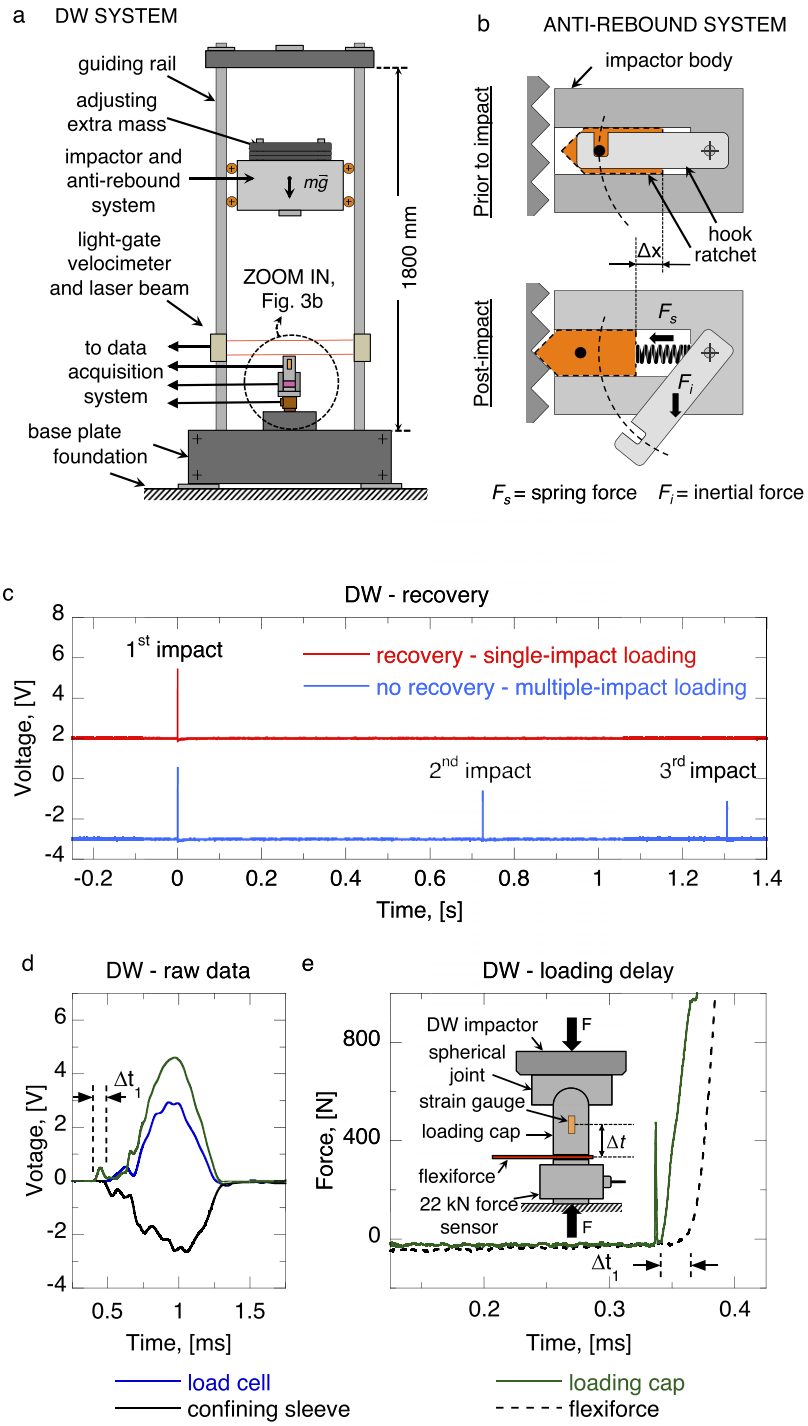

Figure 4. Intermediate strain rate loadings. (a) Schematic of the drop-weight (DW) loading system and its diagnostics. (b) Working principle of the anti-rebound system. (c) DW compressive loadings with recovery and without recovery. (d) Example of raw data. (e) Delay correction between the loading cap and the top loading interface (Δt_1).

perform the compressive loading up to 0.5 mm s^{-1} maximum speed in order to avoid overloading the load cell due to component inertia. The calibration relationships between the measurands and the initial loading conditions (e.g. peak force and crosshead velocity) were obtained from least-squares regression analysis on the data points (appendix 3).

3.5.2. Intermediate strain rate regime

We performed the compressive loadings the intermediate strain rate on a modified DW system. The DW consisted of a frame, two guiding rails, a free-falling impactor, a base plate, and diagnostics (figure 4(a)). The diagnostics included a 22 kN load cell placed below the pressurization chamber, the strain gauge-mounted loading cap and a two-point light-gate velocimeter used to acquire the velocity upon impact. An anti-rebound system was also implemented on the impactor to prevent uncontrolled secondary impacts, and guarantee the recovery of the samples after a single-compressive event (figures 4(b) and (c)). We used the 22 kN load cell

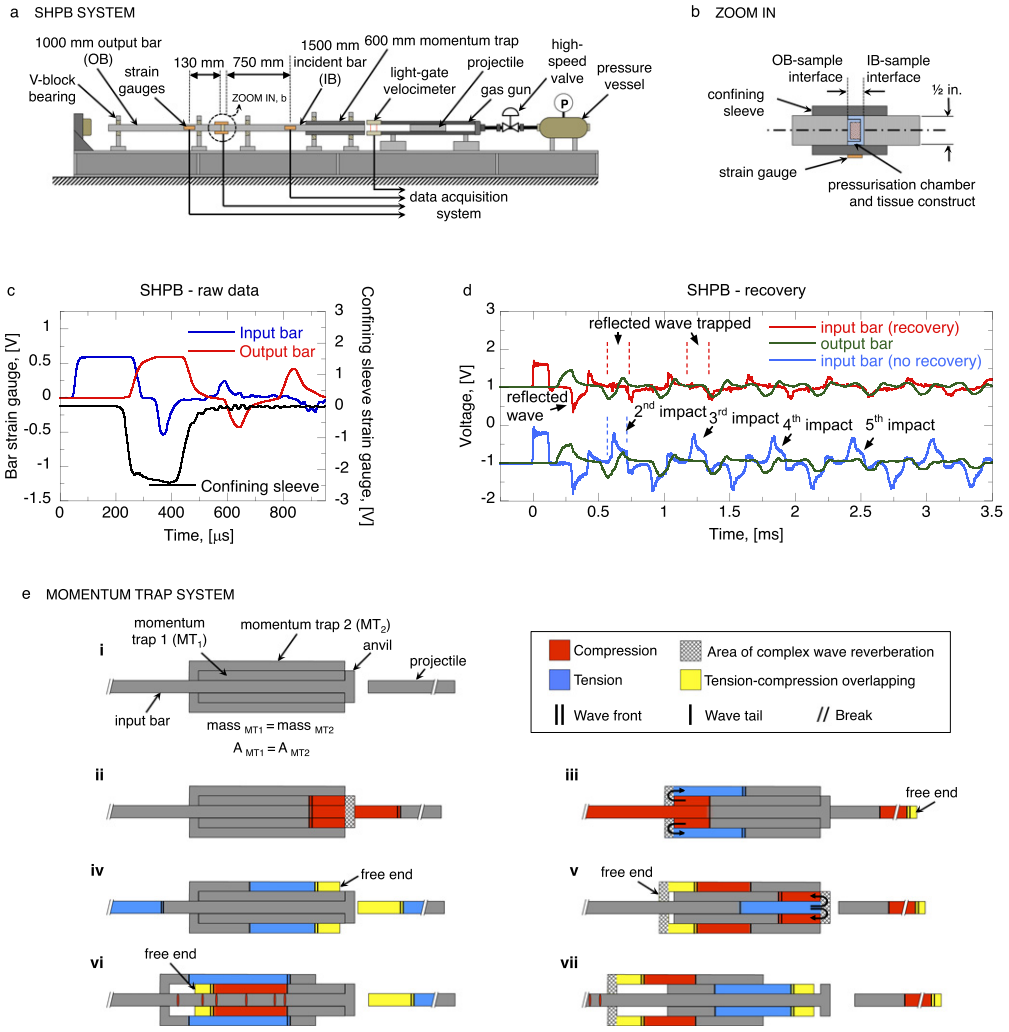

Figure 5. High strain rate loadings. (a) Schematic of the split-Hopkinson pressure bar (SHPB) and its diagnostics. (b) Setup of the pressurization chamber and the confining sleeve. (c) Example of raw data. (d) Examples of SHPB compressive loadings with recovery and without recovery. (e) Working principle of the tandem momentum trap used for dynamic sample recovery. The full description of the momentum trap system can be found in [63].

and the strain gauge-mounted loading cap to obtain the force–time histories at the bottom and top faces of the pressurization chamber, respectively (figure 4(d)). Importantly, because the strain gauge used on the loading cap was positioned at a distance from the sample interface (25 mm) there was a time delay with the 22 kN load cell measurement in the data recording. Whilst this time delay was not critical under the quasi static loading conditions, it became critical under dynamic loading conditions as the loading rate increased. To correct for the time delay, we used a very thin resistive force sensor (Flexiforce Sensor, Tekscan Inc., South Boston, MA, USA) between the loading cap and the 22 kN force sensor to determine the delay and to make the different measurements time coincident (figure 4(e)). Different loading conditions were generated by dropping impactors of varying mass from different heights, and the calibration relationships were determined following the same approach than in the UTF experiments (appendix 3).

3.5.3. High strain rate regime

We performed the high strain rate compressive loadings on a 12.7 mm diameter SHPB apparatus made of 7068 Al Alloy ($\sigma_y = 655$ MPa and $E = 73\,100$ MPa, $\rho = 2\,850$ k m^{-3}, $c_0 = 5\,030$ m s^{-1}) (figure 5(a)). The SHPB setup consisted of a 1500 mm and a 1000 mm long cylindrical bars, called input bar (IB) and output bar (OB), respectively. In an SHPB compression test, the specimen is coaxially sandwiched between the end of the IB and OB (figure 5(b)).

A projectile is launched on the free end of the incident bar generating a longitudinal compression wave with associated strain, ε_I. Upon impact, the incident wave travels within the IB towards the sample. The sample is compressed as the wave travels at the speed of sound across the sample and transmits into the OB with associated strain, ε_T. The compression of the sample is accompanied by a reflected wave, with associated strain ε_R, resulting from the acoustic impedance mismatch between the bar and the sample materials (figure 5(c)). The bars were instrumented

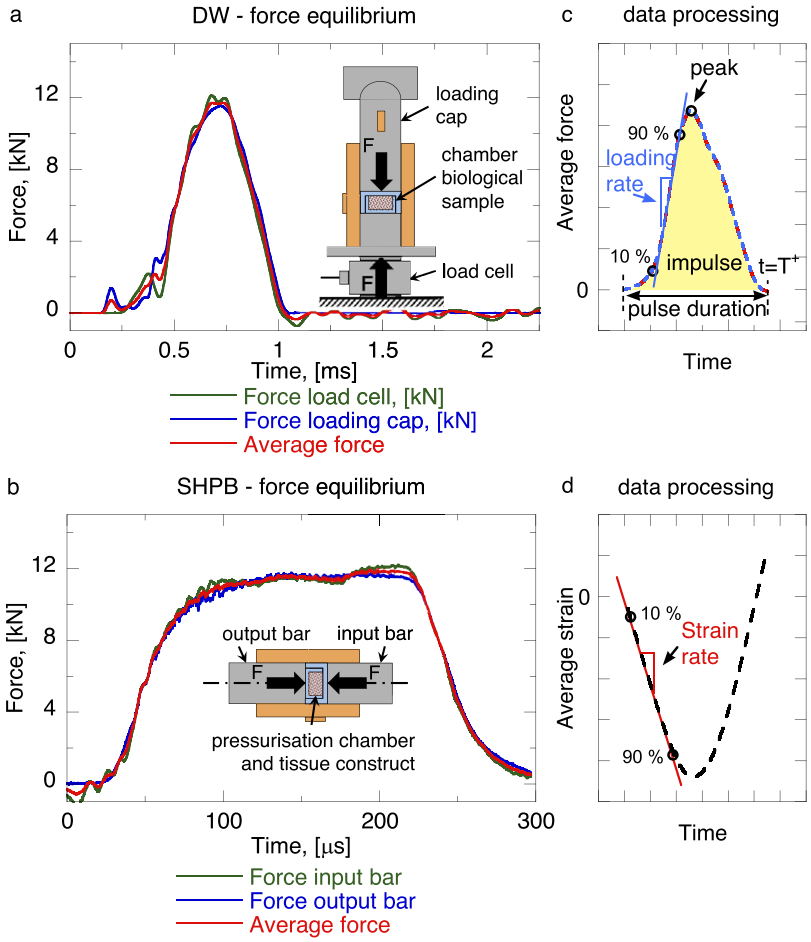

Figure 6. Data processing. (a, b) Dynamic force equilibrium on (a) the DW and on (b) the SHPB. (c) Computation of the mechanical peak force, loading rate and loading impulse from the average axial force–time history. (d) Computation of the average strain rate from the average strain–time history.

with semiconductors strain gauges mounted in pair with the active element parallel to the centreline of the bar to measure the longitudinal strain, and diametrically opposite in order to compensate for any bar bending. The strain gauge pairs were positioned at a distance of 750 mm and 130 mm from the IB- and OB-specimen interfaces, respectively. To allow sample recovery after a single-compressive event, the SHPB apparatus was mounted with a 600 mm long momentum capture system based on the tandem momentum trap for dynamic specimen recovery as proposed by Prot and Cloete [63] (figures 5(d) and (e)). We used a two point light-gate velocimeter to measure the velocity upon impact of the projectile on the IB. The force–time and displacement–time histories at the IB- and OB-specimen interfaces were obtained from the strain–time histories at the bar gauge stations by using the principles of one-dimensional elastic wave propagation in rod bar [64], as:

$$F_{\mathrm{IB}}(t) = A_{\mathrm{b}}E_{\mathrm{b}}\left(\varepsilon_{\mathrm{I}}(t) + \varepsilon_{\mathrm{R}}(t)\right) \tag{3}$$

$$F_{\mathrm{OB}}(t) = A_{\mathrm{b}}E_{\mathrm{b}}\left(\varepsilon_{\mathrm{T}}(t)\right) \tag{4}$$

where A_{b} is the diameter of the bar, E_{b} is the Young's modulus of the bar, F_{IB} and F_{OB} are the force intensity at the IB- and OB-specimen interfaces, respectively. The displacements at the bar-specimen interfaces were calculated as:

$$u_{\mathrm{IB}}(t) = c_{\mathrm{L,bar}}\int_0^t \left(-\varepsilon_{\mathrm{I}}(t) + \varepsilon_{\mathrm{R}}(t)\right)\mathrm{d}t \tag{5}$$

$$u_{\mathrm{OB}}(t) = -c_{\mathrm{L,bar}}\int_0^t \varepsilon_{\mathrm{T}}(t)\,\mathrm{d}t \tag{6}$$

where $c_{\mathrm{L,bar}}$ is the longitudinal sound speed in the bar material, u_{IB} and u_{OB} are the displacements of the IB- and OB-specimen interfaces, respectively. All the strain measurements ε_{I}, ε_{R} and ε_{T} were corrected for dispersion effects according to Gong *et al* [65]. The average strain–time history $\varepsilon(t)$ in the specimen was calculated as:

$$\varepsilon(t) = \frac{u_{\mathrm{IB}}(t) - u_{\mathrm{OB}}(t)}{L_{\mathrm{s}}} \tag{7}$$

where L_{s} is the length of the specimen. We generated different loading conditions by varying the length of the projectile (160, 320, 450 or 560 mm) and its

impact velocity. The impact velocity ranged from 5 to 30 m s^{-1} in order to limit the stress intensity to 70% of the projectile material yield stress (6082-T6 Al alloy with $\sigma_y = 295$ MPa and $E = 72\,000$ MPa, $\rho = 2\,700$ kg m^{-3}, $c_0 = 5\,030$ m s^{-1}), and thereby to ensure the propagation of solely elastic waves in the system according to:

$$0.7\sigma_{y,P} = \frac{1}{2}\rho_P c_{0,P} v_{P,\max} \quad (8)$$

where $\sigma_{y,P}$ is the yield stress, ρ_P is the density, and $v_{P,\max}$ is the maximum impact velocity of the projectile. The calibration relationships between the measurands and the initial impact conditions were obtained from least-squares regression analysis on the data points (appendix 3).

3.6. Mechanical loading parameters

We used the two force–time measurements to verify the process of dynamic equilibrium during the loading and used the average axial force–time history in the data processing (figures 6(a) and (b)). The loading impulse was computed as the area under the average axial force–time profile (figure 6(c)). The axial stress–time history was inferred from the average axial force–time history, and based on the nominal cross-section area of the pressurization chamber. The average hydrostatic pressure P developed within the confining sleeve was computed using the axial and radial stresses, as:

$$P(t) = \frac{(\sigma_a + 2\sigma_\theta)}{3} \quad (9)$$

where σ_a is the axial stress and σ_θ is the radial stress. The average loading rate and average strain rate were calculated as the slope of the linear regression between 10% and 90% of the rising edge of the average axial force–time and average strain–time history profiles, respectively (figures 6(c) and (d)).

3.7. Statistical analysis

The results are reported as mean ± standard deviation of at least three separate experiments ($n = 3$), unless otherwise stated. Statistical significance was analyzed by one-way ANOVA with Tukey post-hoc test to assess differences between sample conditions and treatments. A level of 5% was considered statistically significant in all statistical tests ($p < 0.05$).

4. Calibration and validation of the *in vitro* platforms

4.1. Calibration of the *in vitro* experimental loading platforms

We performed the calibration experiments of the different loading apparatus by exposing a PDMS pressurization chamber containing an acellular agarose tissue constructs to different initial impact conditions. We conveniently used the peak pressure and the pulse duration as measurands in the calibration relationships.

The peak pressure was used to define the ultimate level of mechanical stress to expose the biological samples to. It was additionally useful as '*loading endpoint*' because an identical magnitude of pressure could be consistently performed on the three loading apparatus regardless of the loading regime. This strategy was not possible with the other mechanical characteristics. The peak pressure ranged between 6.2 MPa and 113.5 MPa (figures 7(a), (d) and (g)). On the UTF and DW apparatus, the upper limit of the range was constrained by the apparatus size and the rated capacity of the diagnostics (e.g. load cell). On the SHPB apparatus, it was imposed by the maximum impact velocity.

In conjunction with the pressure, the pulse duration was used to tailor all the time-dependent mechanical parameters, including the loading impulse, the loading rate and the strain rate. The pulse duration ranged from 50 μs on the SHPB to a few seconds on the UTF, as its crosshead velocity was lowered (figures 7(b), (e) and (h)).

4.2. Definition of the parameter space relevant to IED/landmine

Figures 7(c), (f) and (i) shows examples of pressure pulses performed in the three regimes of loading. In addition to applying identical magnitude of peak pressure regardless of the loading regime (e.g. strain rate), the *in vitro* platforms could be used to tailor loading pulses that exhibited other common defining mechanical characteristics (e.g. loading rate, loading impulse). This enabled to elucidate the extent to which the various mechanical features, acting alone or applied in combination with others, affect the response of the biological samples. For instance, under dynamic conditions, this permitted an investigation of the effects of the loading impulse independently of the strain rate, or in a wider operational program, to decouple the effects of the strain rate regime regardless of the mechanical stress. Finally, a series of low-intensity pressure pulses could be applied in series and combined to match the characteristics of a single-impact event applied on a different apparatus (appendix 4). It therefore becomes possible to further explore the resilience and cellular damage threshold to low-pressure multiple loadings as opposed to a single high-pressure event sharing common loading characteristics.

Figure 7 summarizes examples of SHPB, DW and UTF loading conditions in (j) the loading rate-peak axial force, (k) in the impulse-pulse duration and (l) in the strain rate-peak axial stress parameter spaces. Each data point represents an independent compressive loading experiment. The ranges of mechanical loading conditions achievable on the platforms and

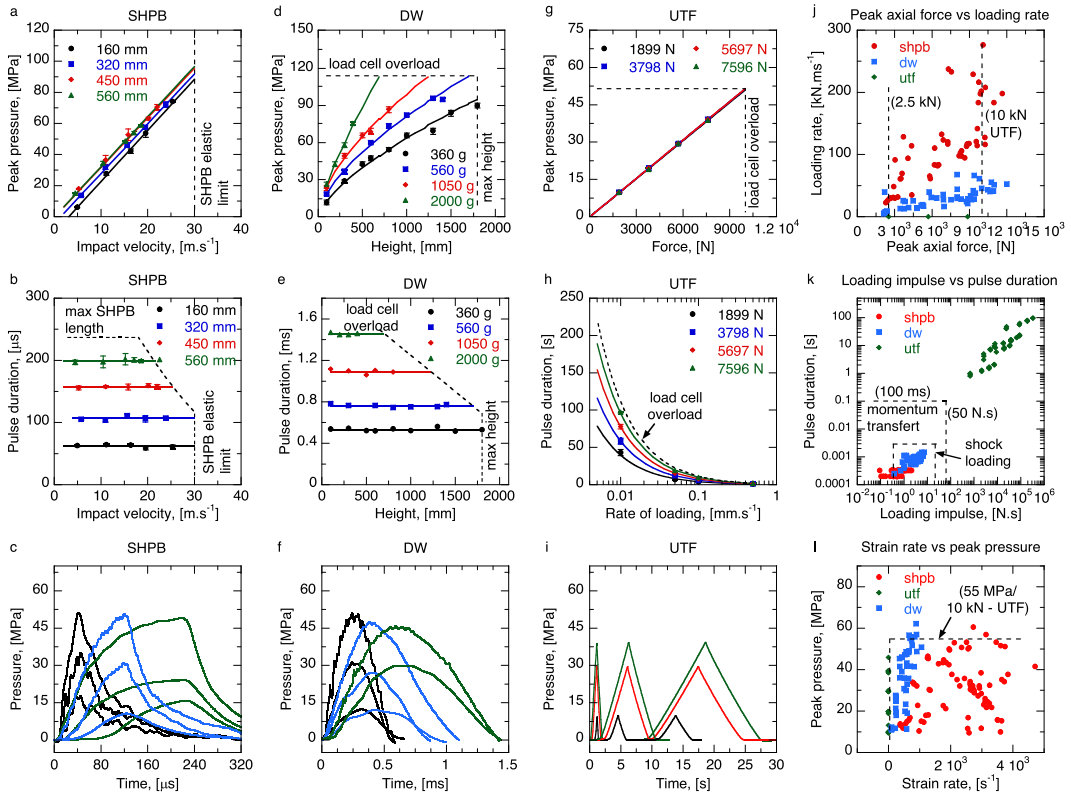

Figure 7. Calibration of the *in vitro* platforms. (a–i) Calibration relationships giving the peak pressure and the pulse duration for different impact loading conditions on the SHPB (a, b), DW (d, e) and the UTF (g, h). (c, f, i) Examples of pressure–time histories on the SHPB (c), the DW (f) and the UTF (i). (j–l) Definition of the mechanical parameter spaces relevant to near-field blast wave exposure. Each point represents an experiment. (j) Loading rate-peak axial force space. (k) Loading impulse-pulse duration space. (l) Strain rate-peak pressure space.

their relevance to blast loading are depicted in the different parameter spaces. The peak force levels ranged between 2.5 kN and 10 kN. The upper limit corresponded to the load cell rated capacity on the UTF. The highest figures of loading rate recorded in landmine/IED blast loading can approach 270 kN ms^{-1}. Similar conditions could be easily replicated on the SHPB apparatus. Lower values of loading rate could also be generated by using the DW and UTF. While most of the blast deformation processes occur under a dynamic regime during the shock loading, the range of strain rate explored during the calibration experiments was set between 10^{-2} and 10^{3} s^{-1}. The loading impulse conditions recorded during the shock loading could be replicated on the DW and the SHPB systems. Finally, the most representative pulse durations of real shock loadings, that varies between 500 μs and a few milliseconds, were relevantly replicated on the DW.

4.3. Effect of the loading on the mechanical properties of the 3D-scaffold

Before conducting the compressive loadings on live biological samples, we verified how the mechanical stress imparted to the biological samples (e.g. hydrogel constructs) would affect their mechanical integrity. We compared the mechanical properties of the hydrogel constructs before and after single-impact compressive loading on the platform. Post-loading, their elastic properties along with their failure parameters were assessed from quasi-static unconfined compression tests on an UTF. The system was corrected for platen parallelism and assessed for compliance. The samples were kept in a hydrated state and loaded up to failure using a ramp phase at 0.001 s^{-1} (appendix 5). The force and displacement–time histories were recorded at a sampling rate of 10 Hz. The compressive modulus was derived from the initial slope of the engineering stress–strain curves between 1% and 2% strain. The stress and the corresponding strain to failure were identified at the peak just before the sharp drop in the engineering stress–strain plot. We used two types of control samples to assess separately the effects of the pressurization chamber and the mechanical loading on the mechanical properties of the hydrogel constructs. The tissue culture (TC) control samples were not setup in the pressurization chamber and not exposed to the mechanical loading. The SHAM samples were setup in the pressurization chamber but not exposed to the mechanical loading. The elastic modulus remained unaffected by the different mechanical loading as compared to the TC and

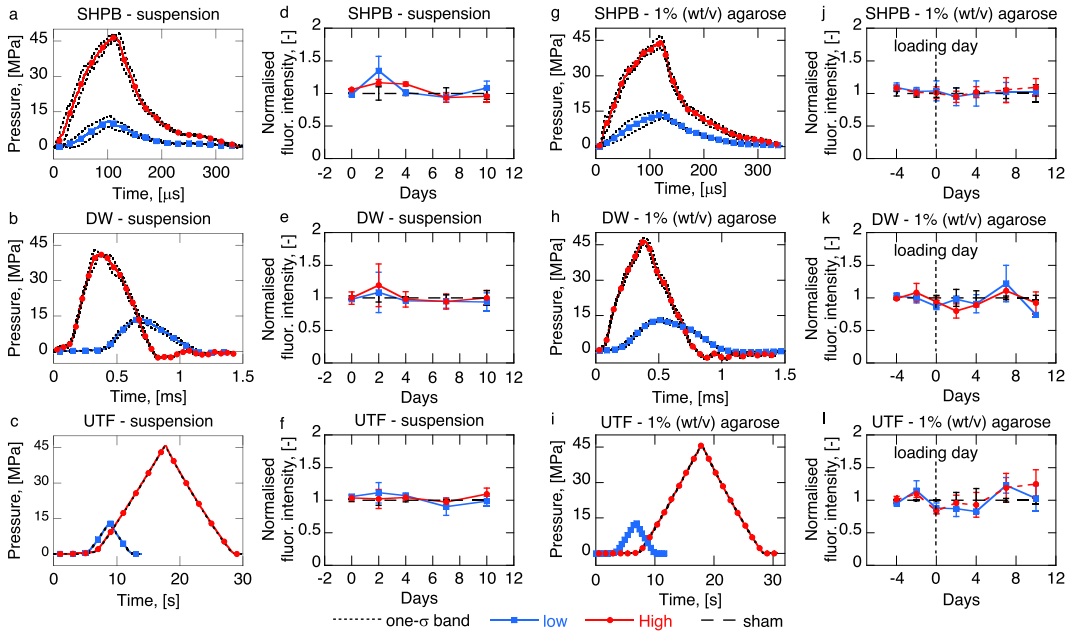

Figure 8. Dynamic loading of MSCs. (a–i) Average pressure–time history in the single-cell suspension experiments (a–c) or in the 1% (wt/v) agarose hydrogel experiments (g–i). Cell health in PO MSCs loaded on the SHPB (d, j), the DW (e, k) and the UTF (f, l). Average data (biological repeats = 4) expressed as mean ± SD. Day 0 corresponds to the day of the compressive loading experiments. Alamar Blue dye reduction in the mechanically-loaded samples is normalised to the SHAM controls.

SHAM samples (appendix 5, $p < 0.05$ for all pair comparisons). We also found that the failure properties (stress and strain) were not affected by either the handling (e.g. SHAM samples), or by the loading (e.g. loaded samples), unless for the stress in the DW loading (appendix 5, control vs DW loaded, p-value = 0.0048; DW SHAM vs DW loaded, p-value = 0.0022).

4.4. Effect of the pressurization chamber on cell viability

We also verified that use of the pressurization chamber did not affect cell health and cell viability, via AlamarBlue assay and Live/Dead assay, respectively. Thus, we encapsulated agarose tissue construct containing PO MSCs in the pressurization chamber (appendix 5) and incubated the biological samples for time periods from 5 up to 180 mins at room temperature. We found that cell health was not affected by the pressurization chamber (T5 vs TC, p-value = 0.8773; T30 vs TC, p-value = 1; T60 vs TC, p-value = 1; T120 vs TC, p-value = 0.1993; T180 vs TC, p-value = 0.6935). The maintenance of cell viability was further confirmed by florescence microscopy by using a Live/Dead assay (appendix 5).

4.5. Dynamic loading of PO MSCs

We exposed PO MSCS in liquid suspensions or encapsulated in hydrogel constructs to different pressure pulses on the SHPB, the DW and the UTF (appendix 6). Depending on the nominal peak pressure intensity, the loading pulses are referred to as low (∼15 MPa, blue) or high (∼45 MPa, red). The mechanical loading histories were tailored with similar peak pressure intensities applied over different ranges of pulse duration: from tens of microseconds to a few seconds (figures 8(a)–(f)). In addition to the similar magnitude of peak pressure, the loading histories also showed continuous overlap of loading parameters, including the strain rate (DW High vs SHPB low), the pulse duration (low vs High), the loading rate (SHPB low and DW High) and the loading impulse (SHPB High and DW low) (appendix 6).

We performed a quantitative Alamar Blue assay to assess the effect of the mechanical loading on cell health. Cell health in PO MSCs was monitored just prior to the compressive loading and on day 2, 4 and 7 post-loading (figures 8(g)–(i)). Post-loading, we found that cell health in both cellular *in vitro* models remained stable in the loaded samples in comparison to the SHAM control.

4.6. Activation of PO MSCs

We assessed the activation of PO MSCs in response to the mechanical using quantitative real time polymerase chain reaction (qRT PCR) (appendix 7). Figure 9(a) compares Runx2 mRNA levels in the loaded PO MSC single-cell suspension samples with respect to the SHAM samples. Twenty-four hours post-loading, we found that only the dynamic loading conditions (SHPB and DW) upregulated Runx2 mRNA in the PO MSCs (SHPB low = 3.12 ± 1.00; SHPB high = 6.76 ± 2.03; DW low = 3.76 ± 1.26; DW high = 4.65 ± 1.14). The quasi-static loading down-regulated or barely upregulated Runx2 mRNA as compared to the SHAM samples (UTF low = 0.95 ± 0.37; UTF High = 1.34 ± 1.09). The results showed that mechanical stimuli of identical nominal

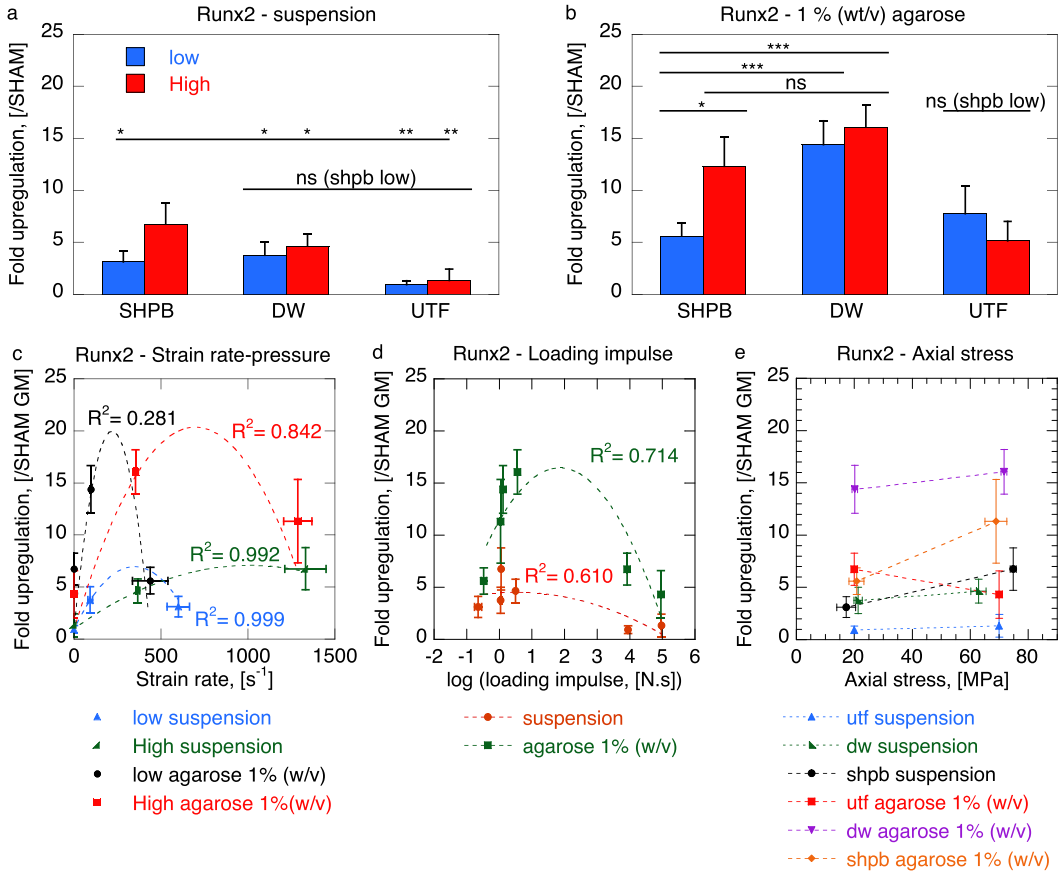

Figure 9. Activation of Runx2 in MSCs under mechanical loading. (a, b) Effects of the strain rate dependent mechanical loadings on Runx2 mRNA expression in PO MSCs. (c–e) Effects of the mechanical parameters on Runx2 mRNA in mechanically-loaded PO MSCs. (c) Strain rate-pressure model. (d) Loading impulse model. (e) Pressure model. Average data (biological repeats = 4) expressed as mean ± SD fold upregulation with respect to the SHAM controls. One-way ANOVA with Tukey post-hoc test ($p < 0.05$).

peak pressure or loading impulse applied under different loading regimes generated statistically different stimulation levels in PO MSCs.

In the agarose-encapsulated hydrogel constructs, PO MSCs upregulated Runx2 mRNA in all loading conditions (SHPB low = 5.61 ± 1.28; SHPB high = 11.33 ± 4.02; DW low = 14.40 ± 2.29; DW high = 16.07 ± 2.13; UTF low = 6.74 ± 1.53; UTF high = 4.32 ± 2.27) (figure 9(b)). Interestingly, no statistical significance was found between the SHPB high and DW low loadings of similar loading impulse ranges, but different strain rate, pulse duration and peak pressure. More importantly, the mechanical stimuli of same peak pressure intensity (but different pulse duration, strain rate regime and loading impulse) did not consistently induce similar levels of upregulation of Runx2 mRNA in PO MSCs.

Figure 9(c) presents the average upregulation levels of Runx2 mRNA measured in PO MSCs as a function of the strain rate for each range of peak pressure and according to the extracellular environment. For a given pressure intensity, the data suggest that there is a value of strain rate that maximised the expression of Runx2 mRNA. For PO MSCs encapsulated in agarose hydrogel, Runx2 mRNA expression levels was maximal at a mechanical stimulus of ∼15 MPa peak pressure applied at an average strain rate of approximately 220 s^{-1}. When the peak pressure increased to ∼45 MPa, the expression of Runx2 mRNA was maximal at an average strain rate of approximately 700 s^{-1}. Therefore, the data suggested that the higher the peak pressure the higher the range of strain rate needed to maximally stimulate the upregulation of Runx2 mRNA. Therefore, this strain rate-pressure model suggested that the cellular activation of PO MSCs was modulated not only by the intensity, but also by the time-dependent characteristics of mechanical stimulus they experience.

Similarly, the loading impulse models also suggested that there was a range of impulse values that maximised the expression of Runx2 mRNA at approximately 1.84 log(N.s) total loading impulse (equivalent to 69.18 N.s) in PO MSCs embedded in 1% (w/v) agarose hydrogel. In single-cell suspension samples, a loading impulse of 0.5 log(N.s) (equivalent to 3.16 N.s) maximised the expression of Runx2 mRNA (figure 9(d)). Finally, we did not find a clear trend between Runx2 mRNA expression and the peak pressure alone (figure 9(e)).

5. Discussion and conclusions

In this study, we designed, developed and calibrated *in vitro* experimental platforms that permit the exposure of biological cells cultures to mechanical conditions mimicking landmine/IED trauma. Using these platforms, we investigated the survival and the cellular activation of PO MSCs under strain-dependent loadings and showed the upregulation of Runx2 mRNA as a function of the mechanical pressure, the strain rate and the loading impulse.

We developed the *in vitro* platforms to apply mechanical stimuli to cells in a 3D microenvironment and in a liquid suspension culture system. A pressurization chamber was manufactured from PDMS owing to its non-cytotoxic properties and its acoustic impedance characteristics promoting efficient transmission of the stress pulses at the chamber-cell environment interface [61]. We considered cost, optical clarity, and ease of manufacture and sterilization in the design of the *in vitro* platforms [57–59]. Particularly, the simple design and the consistent interfacing of the chamber as a single unit on the three experimental loading devices was emphasized. We designed the pressurization chamber as a hermetically sealed volume to maintain the cellular environment under sterile conditions [58] and achieved a throughput of approximately 8 to 10 samples per hour.

The majority of the blast-specific *in vitro* platforms have utilized two-dimensional (2D) culture systems [16, 26, 31, 32, 66], however, the disparities in cell–cell and cell–substrate interactions in cells cultured on flat, non-physiologically stiff materials may, potentially, affect forces perceived by cells and, thereby, the transduction mechanisms as compared to the *in vivo* scenario [67]. Liquid suspension and 3D microenvironments, recapitulating the features of native tissues more closely, may elicit more faithful higher-order cell processes that are inherently 3D, which otherwise might not be observable in 2D culture systems [68]. To our knowledge, this is the first research on the development of *in vitro* platforms that incorporate the features of 3D cell cultures under loading conditions replicating landmine/IED blast trauma.

Central to the development of the *in vitro* platforms was defining reproducible loading histories featuring experimentally quantifiable mechanical parameters. By considering the greater extent of the pathological effects associated to the compressive phase of the shock loading, the platforms were modified to deliver a single-pulse compressive loading only.

The profile of the pressure pulses was tailored to match the description of actual blast loadings in terms of pressure, loading impulse, peak force, strain rate, pulse duration and loading rate. In contrast with already reported blast *in vitro* models (e.g. shock tube), the platforms allowed the investigation of the mechanical characteristics of blast loadings as transmitted in soft tissues, either individually or in combination. Moreover, it is important to note that conventional pressure-based platforms, such as shock tubes, replicate the typical external pressure–time history before it mechanically couples to the samples, but do not capture the loading history transmitted through the samples [16, 24, 66].

In the development of the *in vitro* platforms, we emphasized the broad range of strain rates and the high magnitudes of pressure achievable in the samples as compared to the contemporary *in vitro* models. The latter operate pressure pulses in the range of tens to few hundreds of kilopascals at most, which match the mechanical conditions for addressing primary blast injuries of the hearing, trachea and pulmonary or central nervous systems—anatomical levels at which the blast wave has sufficiently expanded at a distance from the detonation seat [12–14, 17–19, 24]. In contrast, on the *in vitro* platforms described in this study, the cells could be exposed to mechanical stress to nearly one-hundred megapascals relevant to the loading conditions in close proximity to the detonation seat.

PO MSCs are recognized to play a pivotal role in the bone formation process, including the formation of normal, healthy bone tissue during the embryonic development, and the postnatal processes including bone growth, remodeling and fracture repair. In their native form PO MSCs exist in a heterogeneous mix of cells that are all adherent to extracellular matrix via integrin interactions. In this study we have simplified the system by examining homogenous cultures of PO MSCs that are non-adherent. Ultimately, future directions of research need to address more complex, physiologically-relevant biological systems thereby examining the impact of adhesion and a heterogeneous cell environment on the response of PO MSCs to blast.

Agarose hydrogels have been extensively used as encapsulating material to investigate the biological response to defined levels of mechanical loading or deformation in progenitor cells [69–71]. In this study, we used agarose hydrogel to create a simplified 3D cell scaffolding capable of homogeneously distributing and immobilizing the PO MSCs for the short duration of the experiments. We also proposed to use agarose hydrogel as 3D environment to encapsulate cells in 2D monolayer coverslip and tissue explants. We considered its large range of tunable physical and mechanical properties [72], its high porosity [73, 74], along with its non-adherent material characteristics for the encapsulation of the PO MSCs [75, 76]. In this research, we produced agarose hydrogel constructs of 1% (w/v) final concentration in order to mimic a scaffold of compressive modulus falling within the range of figures reported for muscle tissue (∼15 kPa) [77, 78]. This was chosen as the development of blast-mediated HO has been principally

reported in traumatized soft tissues, such as muscle and ligament [79].

We applied a range of predefined mechanical stimuli to PO MSCs in liquid suspension or 3D hydrogels. Firstly, we demonstrated that cell health of PO MSCs, whether encapsulated in the hydrogel construct or in single-cell liquid suspension, was not affected by large loading impulse (e.g. on the UTF) and by dynamic single-impact loading applied at higher strain rates (e.g. on the DW and the SHPB). A body of literature has investigated the effects of hydrostatic pressure beyond 300 MPa applied under quasi-static conditions to various cell types, as reviewed in [80]. However, limited investigation has been conducted on the functionality and integrity of MSCs at high strain rates. Our data indicated that PO MSCs are very resilient to rapid changes in pressure [81].

While keeping the peak pressure constant, we changed the rate of loading along with the duration of the mechanical stimuli to study the cellular activation of PO MSCs throughout the expression of Runx2 mRNA. Runx2 is a Runt domain-containing, DNA-binding transcription factor that is described as the master transcription factor for the production and maintenance of progenitors cells, and their transition into immature osteoblasts [82]. It regulates the commitment of progenitor cells to the osteoblastic lineage during the early stage of both endochondral and intramembraneous ossification [82, 83]. In this study, we measured Runx2 mRNA expression levels as a proof of concept of cellular activation relevant to MSC differentiation by high rates of loading.

Twenty-four hours post-loading, we showed that PO MSCs upregulated the expression of the Runx2 mRNA to different levels depending on the loading history and the extracellular microenvironment. Our data indicated that cellular activation was neither solely dependent, nor directly proportional to the magnitude of a single parameter, such as the loading duration, the pressure or even the loading impulse. Our data suggested that cellular activation in PO MSCs resulted from the combined action of several factors, including the pressure and the strain rate. Finally, PO MSCs showed differences in Runx2 mRNA expression levels depending upon the extracellular microenvironment used to convey the pressure wave (i.e. liquid or hydrogel). This finding is consistent with the well-known fact that, increasing the stiffness of the extracellular environment, enhances the osteogenic response of MSCs to mechanical stimuli [78]. The results presented in this paper are consistent with the known effect of blast loadings from IEDs and landmines in promoting HO. One caveat of the study regarded the small sample size and the limited loading conditions per platform and across stain rate regimes. Further experiments containing multiple groups of loading conditions, and more biological replicates are needed to bring informative details of the proposed models. Although, we did not find experimental evidence of such models in other studies, second order polynomial fittings were arbitrarily adjusted on the three data points of each set and appeared to be consistent in the data sets. More data collection and subsequent multivariate analyses are required to determine the validity of the proposed models. Another limitation of this study is that we have solely investigated changes in the expression of Runx2 mRNA 24 h after cellular loadings. Further research is therefore required to delineate the signaling pathways activated by non-physiological mechanical loading and, subsequently, leading to Runx2 mRNA activation and determine whether high strain rate loading strategies sufficient in inducing osteogenesis exist. Similarly, future work is warranted to investigate whether other key osteogenic genes are upregulated at a later time (weeks) and indeed whether MSCs exhibit physical characteristics of osteoblasts at these later times.

In summary, this paper is the first research introducing and validating *in vitro* platforms capable of replicating loading conditions in 3D culture systems as recorded in IED/landmine blast avulsion of lower extremities. The capability of decoupling the mechanical features defining blast loading allowed us to examine the combinatorial and singular effects of the different features of blast insults on PO MSCs. We have investigated how the effects of single-pulse loadings of high pressure applied over a wide range of strain rate affected the maintenance of cell health, and the cellular response as measured by upregulated Runx2 mRNA transcription factor, which is pivotal in numerous cellular and biomolecular pathways. This proof of concept establishes a new window to address fundamental questions regarding IED/landmine blast biomechanics in screening a wide variety of cellular types and tissues.

Author contribution

W G P and S M R conceived the project idea which was developed into an experimental model by D R S. D R S conceived the method and conducted the experiments with support from H D A and D J C. D R S drafted the manuscript and all authors reviewed, edited and approved of the final version.

Availability of materials and data

The datasets and materials generated during and analyzed during the current study are available from the corresponding author on reasonable request.

Competing interests

The authors declare no competing interests.

Acknowledgments

This work was conducted under the auspices of the Royal British Legion Centre for Blast Injury Studies at Imperial College London. The authors would like to acknowledge the financial support of the Royal British Legion. We wish to thank Satpal Sangha, Dr David L Mack and the Blackett Laboratory Physics Workshop for their technical support. The Facility for Imaging by Light Microscopy (FILM) at Imperial College London is part supported by funding from the Wellcome Trust (grant 104931/Z/14/Z) and BBSRC (grant BB/L015129/1).

Role of the funding source

Funders: Royal British Legion—Center for Blast Injury Studies, Imperial College London. The funders had no role in the study design; in the collection, the analysis and the interpretation of the data; in the writing of the manuscript; and in the decision to submit the article for publication.

ORCID iDs

David R Sory https://orcid.org/0000-0003-3392-9353

References

[1] MacDonald J, Lockwood J R, McFee J, Altshuler T, Broach T, Carin L, Harmon R, Rappaport C, Scott W and Weaver R 2003 *Alternatives for Landmine Detection* (Santa Monica, CA: RAND Corporation) (https://www.rand.org/content/dam/rand/pubs/monograph_reports/MR1608/MR1608.pref.pdf)

[2] Ramasamy A, Hughes A, Carter N and Kendrew J 2013 The effects of explosion on the musculoskeletal system *Trauma* **15** 128–39

[3] Owens B D, Kragh J F, Wenke J C, Macaitis J, Wade C E and Holcomb J B 2008 Combat wounds in Operation Iraqi Freedom and Operation Enduring Freedom *J. Trauma Acute. Care. Surg.* **64** 295–9

[4] Ramasamy A, Harrisson S, Lasrado I and Stewart M P M 2009 A review of casualties during the Iraqi insurgency 2006-a British field hospital experience *Injury* **40** 493–7

[5] Potter B K, Burns T C, Lacap A P, Granville R and Gajewski D A 2007 Heterotopic ossification following traumatic and combat-related amputations *J. Bone Jt. Surg. Am.* **89** 476–86

[6] Alfieri K A, Forsberg J A and Potter B K 2012 Blast injuries and heterotopic ossification *Bone Joint Res.* **1** 174–9

[7] Davis T A, O'Brien F P, Anam K, Grijalva S, Potter B K and Elster E A 2011 Heterotopic ossification in complex orthopaedic combat wounds *J. Bone Jt. Surg. Am.* **93** 1122–31

[8] Potter B K *et al* 2010 Heterotopic ossification following combat-related trauma *J. Bone Jt. Surg. Am.* **92** 74–89

[9] Du V, Richard S, Mary G, Gay C, Mazuel F, Reffay M, Menasché P, Agbulut O and Wilhelm C 2017 A 3D magnetic tissue stretcher for remote mechanical control of embryonic stem cell differentiation *Nat. Commun.* **8** 400

[10] Llucià-Valldeperas A, Bragós R, Soler-Botija C, Roura S, Gálvez-Montón C, Prat-Vidal C, Perea-Gil I and Bayes-Genis A 2018 Unravelling the effects of mechanical physiological conditioning on cardiac adipose tissue-derived progenitor cells in vitro and in silico *Sci. Rep.* **8** 499

[11] Cochis A, Grad S, Stoddart M J, Farè S, Altomare L, Azzimonti B, Alini M and Rimondini L 2017 Bioreactor mechanically guided 3D mesenchymal stem cell chondrogenesis using a biocompatible novel thermo-reversible methylcellulose-based hydrogel *Sci. Rep.* **7** 45018

[12] Cho S I *et al* 2013 Mechanisms of hearing loss after blast injury to the ear *PloS One* **8** e67618

[13] Yokoi H and Yanagita N 1984 Blast injury to sensory hairs: a study in the guinea pig using scanning electron microscopy *Arch. Otorhinolaryngol.* **240** 263–70

[14] Newman A J, Hayes S H, Rao A S, Allman B L, Manohar S, Ding D, Stolzberg D, Lobarinas E, Mollendorf J C and Salvi R 2015 Low-cost blast wave generator for studies of hearing loss and brain injury: blast wave effects in closed spaces *J. Neurosci. Methods* **242** 82–92

[15] Barnett-Vanes A, Sharrock A, Eftaxiopoulou T, Arora H, Macdonald W, Bull A M and Rankin S M 2016 CD43Lo classical monocytes participate in the cellular immune response to isolated primary blast lung injury *J. Trauma Acute Care Surg.* **81** 500–11

[16] Arun P, Spadaro J, John J, Gharavi R B, Bentley T B and Nambiar M P 2011 Studies on blast traumatic brain injury using in-vitro model with shock tube *Neuroreport* **22** 379–84

[17] Ahlers S T, Vasserman-Stokes E, Shaughness M C, Hall A A, Shear D A, Chavko M, McCarron R M and Stone J R 2012 Assessment of the effects of acute and repeated exposure to blast overpressure in rodents: toward a greater understanding of blast and the potential ramifications for injury in humans exposed to blast *Front. Neurol.* **3** 32

[18] Miller A P, Shah A S, Aperi B V, Budde M D, Pintar F A, Tarima S, Kurpad S N, Stemper B D and Glavaski-Joksimovic A 2015 Effects of blast overpressure on neurons and glial cells in rat organotypic hippocampal slice cultures *Front. Neurol.* **6** 20

[19] Reneer D V, Hisel R D, Hoffman J M, Kryscio R J, Lusk B T and Geddes J W 2011 A multi-mode shock tube for investigation of blast-induced Traumatic brain injury *J. Neurotrauma* **28** 95–104

[20] Ravin R, Blank P S, Steinkamp A, Rappaport S M, Ravin N, Bezrukov L, Guerrero-Cazares H, Quinones-Hinojosa A, Bezrukov S M and Zimmerberg J 2012 Shear forces during blast, not abrupt changes in pressure alone, generate calcium activity in human brain cells *PLoS One* **7** 39421

[21] Chandra N, Ganpule S, Kleinschmit N N, Feng R, Holmberg A D, Sundaramurthy A, Selvan V and Alai A 2012 Evolution of blast wave profiles in simulated air blasts: experiment and computational modeling *Shock Waves* **22** 403–15

[22] Kuriakose M, Skotak M, Misistia A, Kahali S, Sundaramurthy A and Chandra N 2016 Tailoring the blast exposure conditions in the shock tube for generating pure, primary shock waves: the end plate facilitates elimination of secondary loading of the specimen *PLoS One* **11** e0161597

[23] Logan N, Arora H and Higgins C A 2017 Evaluating primary blast effects in vitro *J. Vis. Exp.* **127** e55618

[24] Nguyen T-T N, Wilgeroth J M and Proud W G 2014 Controlling blast wave generation in a shock tube for biological applications *J. Phys.: Conf. Ser.* **500** 142025

[25] Eftaxiopoulou T, Barnett-Vanes A, Arora H, Macdonald W, Nguyen T T, Itadani M, Sharrock A E, Britzman D, Proud W G, Bull A M and Rankin S M 2016 Prolonged but not short-duration blast waves elicit acute inflammation in a rodent model of primary blast limb trauma *Injury* **47** 625–32

[26] Vandevord P J, Leung L Y, Hardy W, Mason M, Yang K H and King A I 2008 Up-regulation of reactivity and survival genes in astrocytes after exposure to short duration overpressure *Neurosci. Lett.* **434** 247–52

[27] Laplaca M C, Cullen D K, Mcloughlin J J and Cargill R S 2005 High rate shear strain of three-dimensional neural cell

cultures: a new in vitro traumatic brain injury model *J. Biomech.* **38** 1093–105
[28] Chen Y C, Smith D H and Meaney D F 2009 In-vitro approaches for studying blast-induced traumatic brain injury *J. Neurotrauma* **26** 861–76
[29] Bernick K B, Prevost T P, Suresh S S and Socrate S 2010 Mechanical loading of neurons and astrocytes with application to blast traumatic brain injury *27th Army Science Conf. (ASC) (Orlando, FL, 29 November - 2 December 2010)*
[30] Bernick K B, Prevost T P, Suresh S and Socrate S 2011 Biomechanics of single cortical neurons *Acta Biomater.* **7** 1210–9
[31] Bo C, Williams A, Rankin S, Proud W G and Brown K A 2014 Integrated experimental platforms to study blast injuries: a bottom-up approach *J. Phys.: Conf. Ser.* **500** 102001
[32] Nienaber M, Lee J S, Feng R and Lim J Y 2011 Impulsive pressurization of neuronal cells for traumatic brain injury study *J. Vis. Exp.* **56** e2723
[33] Sory D R, Areias A C, Overby D R and Proud W G 2017 Novel method to dynamically load cells in 3D-hydrogels culture for blast injury studies *AIP Conf. Proc.* **1793** 140003
[34] Canchi S, Sarntinoranont M, Hong Y, Flint J J, Subhash G and King M A 2017 Simulated blast overpressure induces specific astrocyte injury in an ex vivo brain slice model *PLoS One* **12** e0175396
[35] Günther M, Plantman S, Gahm C, Sondén A, Risling M and Mathiesen T 2014 Shock wave trauma leads to inflammatory response and morphological activation in macrophage cell lines, but does not induce iNOS or NO synthesis *Acta Neurochir.* **156** 2365–78
[36] Cronin D S, Williams K, Bass C R, Magnan P, Dosquet F, Bergeron D M and van Bree J L M J 2003 Test method for protective footwear against AP mine blast *NATO Joint AVT-HFM Symp. (Koblenz, Germany, 19–22 May 2003)*
[37] Trimble K and Clasper J 2001 Anti-personnel mine injury; mechanism and medical management *J. R. Army Med. Corps* **147** 73–9
[38] Anonym 2004 Test methodologies for personal protective equipment against anti-personnel mine blast *Final Technical Report NATO HFM089/TG024* (Neuilly-Sur-Seine: NATO Research and Technology Organization)
[39] Nechaev E A, Gritsanov A I, Fomin N F and Minnullin I P 1995 *Mine Blast Trauma—Experience from the War in Afghanistan* (St. Petersburg: Vreden Research Institute of Traumatology, Russian Ministry of Public Health and Medical Industry)
[40] Bergeron D M, Anderson I B, Coley G G and Fall R W 2006 Assessment of lower leg injury from land mine blast – Phase 1: test results using a frangible surrogate leg with assorted protective footwear and comparison with cadaver test data *DRDC Suffield TR 2006-051* (Medicine Hat, AB: Defence R & D Canada – Suffield) (https://www.gichd.org/fileadmin/GICHD-resources/rec-documents/AssessmentLowerLeg1.pdf)
[41] Frem D 2019 Estimating the metal acceleration ability of high explosives *Def. Technol.* **16** 225–31
[42] Mott N F 2006 A theory of the fragmentation of shells and bombs *Fragmentation of Rings and Shells. Shock Wave and High Pressure Phenomena* (Berlin: Springer) pp 243–94
[43] Gurney R W 1943 The initial velocities of fragments from bombs, shell, grenades *Ballistic Research Laboratories Report No. 405* (Aberdeen, MD: Aberdeen Proving Ground)
[44] Proud W G 2013 The physical basis of explosion and blast injury processes *J. R. Army Med. Corps* **159** i4–9
[45] Ramasamy A, Hill A M, Masouros S D, Gibb I, Bull A J M and Clasper J C 2011 Blast-related fracture patterns: a forensic biomechanical approach *J. R. Soc. Interface* **8** 689–98
[46] Lee E, Horning H and Kury J 1968 Adiabatic expansion of high explosive detonation products *Technical Report TID 4500-UCRL 50422* (Livermore, CA: Lawrence Livermore National Laboratory, University of California) (https://doi.org/10.2172/4783904)
[47] Lee E, Finger M and Collins W 1973 JWL equation of state coefficients for high explosives *Technical Report UCID-16189* (Livermore, CA: Lawrence Livermore National Laboratory, University of California) (https://doi.org/10.2172/4479737)
[48] Smith P D and Hetherington J G 1994 *Blast and Ballistic Loading of Structures* (Oxford, UK: Butterworth-Heineman)
[49] Harris R M, Rountree M S, Griffin L V, Haida R A, Bice T and Mannion S J 2000 Final Report of the Lower Extremity Assessment Program (LEAP 99-2) (U.S. Army Comunications)vol 2
[50] Clasper J and Ramasamy A 2013 Traumatic amputations *Br. J. Pain* **7** 67–73
[51] Hull J B and Cooper G J 1996 Pattern and mechanism of traumatic amputation by explosive blast *J. Trauma* **40** 198–205
[52] Bergeron D M, Coley G G, Fall R W and Anderson I B 2007 Assessment of lower leg injury from land mine blast – Phase 2: follow up tests with a modified frangible surrogate lower leg and comparison with cadaver test data *DRDC Suffield TR 2007–070* (Medicine Hat, AB: Defence R & D Canada – Suffield) (https://www.gichd.org/fileadmin/GICHD-resources/rec-documents/AssessmentLowerLeg2.pdf)
[53] van der Horst M J, Dijkstra M H, van de Kasteele R M and Luiting Kol M 2008 Blast performance of commercially available demining footwear: a summary of experimental trials on surrogate legs *TNO Report TNO-DV 2008 A379* (Rijswijk: TNO Defence, Security and Safety) (https://apps.dtic.mil/sti/pdfs/ADA494132.pdf)
[54] Harris R M, Griffin L V, Hayda R A, Rountree M S, Bryant R G, Rossiter N D and Mannion S J 1999 The effects of antipersonnel blast mines on the lower extremity *1999 IRCOBI Conf. (Sitges, Spain, 23–24 September 1999)* (Zurich: International Research Council on Biomechanics of Injury) pp 457–67 (http://www.ircobi.org/wordpress/downloads/irc1999/pdf_files/1999_33.pdf)
[55] Footner M J, Bergeron D M and Swinton R J 2006 Development and calibration of a frangible leg instrumented for compression and bending *Technical Report DSTO-TR-1829* (Edinburgh, Australia: Weapons Systems Division Defence Science and Technology Organisation)
[56] Hayda R, Harris R M and Bass C D 2004 Blast injury research: modeling injury of landmines, bullets, and bombs *Clin. Orthop. Rel. Res. Num.* **422** 97–108
[57] Whitesides G M 2006 The origins and the future of microfluidics *Nature* **442** 368–73
[58] Leclerc E, Sakai Y and Fujii T 2003 Cell culture in 3-dimensional microfluidic structure of PDMS (polydimethylsiloxane) *Biomed. Microdevices* **5** 109–14
[59] Kim E, Xia Y and Whitesides G M 1995 Polymer microstructures formed by moulding in capillaries *Nature* **376** 581–4
[60] Khanafer K, Duprey A, Schlicht M and Berguer R 2009 Effects of strain rate, mixing ratio, and stress–strain definition on the mechanical behavior of the polydimethylsiloxane (PDMS) material as related to its biological applications *Biomed. Microdevices.* **11** 53–8
[61] Rahman M F A, Arshad M R, Manaf A A and Yaacob M I H 2012 The effect of different parameter on the flow response of microfluidic-based acoustic sensor *Indian J. Geo-Mar. Sci.* **41** 557–62
[62] Chianese R B and Erdlac R J 1988 The general solution to the distribution of stresses in a circular ring compressed by two forces acting along a diameter *Q. J. Mech. Appl. Math.* **41** 239–47
[63] Prot M and Cloete T J 2016 A tandem momentum trap for dynamic specimen recovery during split Hopkinson pressure bar testing of cancellous bone *J. Dyn. Behavior Mater.* **2** 50–8

[64] Gama B G, Lopatnikov S L and Gillespie J W 2004 Hopkinson bar experimental technique: A critical review *Appl. Mech. Rev.* **57** 223–50
[65] Gong J C, Malvern L E and Jenkins D A 1990 Dispersion investigation in the split Hopkinson pressure bar *J. Eng. Mater. Technol.* **112** 309–14
[66] Effgen G B, Hue C D, Vogel E 3rd, Panzer M B, Meaney D F, Bass C R and Morrison B3rd 2012 A multiscale approach to blast neurotrauma modeling: Part II: methodology for inducing blast injury to in vitro models *Front. Neurol.* **3** article 23
[67] Caliari S R and Burdick J A 2016 A practical guide to hydrogels for cell culture *Nat. Methods* **13** 405–14
[68] Baker B M and Chen C S 2012 Deconstructing the third dimension - how 3D culture microenvironments alter cellular cues *J. Cell Sci.* **125** 3015–24
[69] Lee D A, Noguchi T, Frean S P, Lees P and Bader D L 2000 The influence of mechanical loading on isolated chondrocytes seeded in agarose constructs *Biorheology* **37** 149–61
[70] Mauck R L, Byers B A, Yuan X and Tuan R S 2007 Regulation of cartilaginous ECM gene transcription by chondrocytes and MSCs in 3D culture in response to dynamic loading *Biomech. Model. Mechanobiol.* **6** 113–25
[71] Huang A H, Farrell M J and Mauck R L 2010 Mechanics and mechanobiology of mesenchymal stem cell-based engineered cartilage *J. Biomech.* **43** 128–36
[72] Gasperini L, Mano J F and Reis R L 2014 Natural polymers for the microencapsulation of cells *J. R. Soc. Interface* **11** 20140817
[73] Rahfoth B, Weisser J, Sternkopf F, Aigner T, von der Mark K and Bräuer R 1998 Transplantation of allograft chondrocytes embedded in agarose gel into cartilage defects of rabbits *Osteoarthritis Cartilage* **6** 50–65
[74] Narayanan J, Xiong J-Y and Liu X-Y 2006 Determination of agarose gel pore size: Absorbance measurements vis a vis other techniques *J. Phys.: Conf. Ser.* **28** 83–6
[75] Dang S M, Gerecht-Nir S, Chen J, Itskovitz-Eldor J and Zandstra P W 2004 Controlled, scalable embryonic stem cell differentiation culture *Stem Cells* **22** 275–82
[76] Tung P S, Burdzy K, Wong K and Fritz I B 1992 Competition between cell-substratum interactions and cell-cell interactions *J. Cell. Physiol.* **152** 410–21
[77] Buxboim A, Ivanovska I L and Discher D E 2010 Matrix elasticity, cytoskeletal forces and physics of the nucleus: how deeply do cells 'feel' outside and in? *J. Cell Sci.* **23** 297–308
[78] Engler A J, Sen S, Sweeney H L and Discher D E 2006 Matrix elasticity directs stem cell lineage specification *Cell* **126** 677–89
[79] Barfield W R, Holmes R E and Hartsock L A 2017 Heterotopic ossification in trauma *Orthop. Clin. North Am.* **48** 35–46
[80] Frey B, Janko C, Ebel N, Meister S, Schlücker E, Meyer-Pittroff R, Fietkau R, Herrmann M and Gaipl U S 2008 Cells under pressure - treatment of eukaryotic cells with high hydrostatic pressure, from physiologic aspects to pressure induced cell death *Curr. Med. Chem.* **15** 2329–36
[81] Bo C, Balzer J, Godfrey S, Francois M, Saffell J L, Rankin S M, Proud W G and Brown K A 2012 Pressure pulse induced-damage in live biological samples *EPJ Web Conf.* **26** 03006
[82] James A W 2013 Review of signaling pathways governing MSC osteogenic and adipogenic differentiation *Scientifica* **2013** 684736
[83] Bruderer M, Richards R G, Alini M and Stoddart M 2014 Role and regulation of RUNX2 in osteogenesis *J. Euro. Cell Mater.* **28** 269–86